ROYAL SOCIETY
OF CHEMISTRY

## PAPER

Check for updates

# Concussive injuries induce neuronal stress-dependent tau mislocalization to dendritic spines with acrolein and functional network alteration in TBI-on-a-chip

Edmond A. Rogers, [iD] †[abcd] Tyler C. Diorio,†[a] Timothy Beauclair,[abc]
Jhon Martinez, [iD] [abc] Shatha J. Mufti,[abc] David Kim,[a] Nikita Krishnan,[abc]
Vitaliy Rayz*[ae] and Riyi Shi [iD] *[abc]

Traumatic brain injuries (TBIs) are a risk factor for Alzheimer's disease (AD), and share several important pathological features including the development of neurofibrillary tangles (NFT) of tau protein. While this association is well established, the underlying pathogenesis is poorly defined and current treatment options remain limited, necessitating novel methods and approaches. In response we developed "TBI-on-a-chip", an *in vitro* trauma model utilizing murine cortical networks on microelectrode arrays (MEAs), capable of reproducing clinically relevant impact injuries while providing simultaneous morphological and electrophysiological readout. Here, we incorporate a digital twin of the TBI-on-a-chip model to resolve cell-scale mechanical deformation *via* shear stresses and demonstrate direct connections between impact forces with aberrations in tau and synaptic deficits, and correlate these changes with elevations of oxidative stress, a suspected key contributor to both trauma and neurodegeneration. This multi-disciplinary investigation combines computational modeling, electrophysiology, and imaging, to explore tau mislocalization and functional deficits as a function of force, in the context of a potential mechanism *via* acrolein. We hope that this novel, integrative approach will help improve our mechanistic understanding of trauma and neurodegeneration, solo and in concert, and ultimately assist in generating more effective treatment options.

## Introduction

Post-traumatic brain injury (TBI) and Alzheimer's disease (AD) pose profound financial and societal impacts for all facets of our society.[1–4] While clinical studies have confirmed TBI as a risk factor for AD, the pathogenic mechanisms remain largely unknown and treatment options are limited. Further, the majority of TBIs are mild (mTBI) with limited initial symptoms,[5] often delaying diagnosis and permitting the condition to worsen through biochemical secondary injuries, culminating in neurodegeneration such as AD. Therefore, the identification of critical and targetable post-traumatic secondary injury mechanisms that could lead to

AD is of great importance, an undertaking which will undoubtedly necessitate multidisciplinary efforts at all levels. These integrative approaches will be crucial towards enhancing our understanding of the pathogenesis, facilitating earlier diagnoses, establishing effective therapeutics, and ultimately benefitting patients, their families, and society as a whole.

To date, mechanistic investigations into both TBI and AD have largely been performed in animal models, which emulate important pathological features. However, the relatively low resolutions inherent to *in vivo* studies have limited our ability to discern key molecular pathways linking TBI with AD, especially with regards to trauma-induced biochemical (termed "secondary") injuries, which represent a prime target for intervention.[6] This is particularly evident in head trauma investigations, which can be fraught with compounding variables outside of the investigator's control. In contrast, *in vitro* methodologies offer a simplified and well-controlled approach for isolating variables of interest, which could provide an effective tool to unravel the complex interplay of pathogenic pathways between TBI and AD.

In an effort to respond to this unmet need, we recently developed "TBI-on-a-chip", an *in vitro* model capable of

[a] *Weldon School of Biomedical Engineering, Purdue University, West Lafayette, IN 47907, USA. E-mail: vrayz@purdue.edu, riyi@purdue.edu*
[b] *Department of Basic Medical Sciences, School of Veterinary Medicine, Purdue University, West Lafayette, IN 47907, USA*
[c] *Center for Paralysis Research, Purdue University, West Lafayette, IN 47907, USA*
[d] *Indiana University School of Medicine, Indianapolis, IN, 46033, USA*
[e] *School of Mechanical Engineering, Purdue University, West Lafayette, IN 47907, USA*
† Co-first authorship.

recapitulating multiple key *in vivo* components of both TBI and AD pathologies, representing a novel preparation uniquely capable of mechanistically exploring the potential connection between TBI, AD, and neurodegeneration.[7–9] At clinically-relevant injury forces, TBI-on-a-chip has demonstrated impact-induced elevations of both acrolein, a key aldehyde and a marker of oxidative stress that has been implicated in TBI and AD, and Aβ42 aggregation, a hallmark of AD pathogenesis.[9–12] Further evidence suggests that acrolein may have a causative role in inflammation and Aβ42 aggregation, with corresponding deficits in network electrical activity determined with microelectrode array (MEA) recording technology.[9] These results not only suggest key molecular pathways linking TBI with AD, but also illustrate the capabilities of this novel TBI-on-a-chip system.

In addition to Aβ pathologies, the disruption of tau has also emerged as a key factor contributing to AD in both clinical and preclinical animal studies,[13–15] particularly in regards to chronic traumatic encephalopathy (CTE), a disease characterized by repeated TBI with neuropathological features similar to AD.[16] Further, recent studies have revealed a link between neuronal stretch injury with tau displacement and synaptic loss, morphological features thought to directly precede the neurofibrillary tangles that, along with amyloid pathologies, pathologically define AD.[17,18] With clinically relevant mechanical concussive impact injuries, superior spatial–temporal resolution, and electrophysiological capabilities, the TBI-on-a-chip system is well suited to further this investigation, more specifically, to investigate the role of tau and quantitatively describe its relationship with force, acrolein, and alterations in synaptic architecture and function, in the context of TBI and with regards to Aβ pathologies.

A critical concern of TBI is the mechanistic coupling between mechanical forces and tissue injury. It is well established that the initial, primary injury triggers and dictates the magnitude, and spatial and temporal nature of the resulting secondary injuries, which in concert produce the final outcomes of TBI.[10,11,19,20] Therefore, understanding the mechanical forces initially experienced by neurons at the cellular level is of great importance to quantitatively link primary with secondary injuries, and more acutely determine the final pathological outcomes as a function of initial impact. While similar investigations have been attempted in animal models, we feel that TBI-on-a-chip, with its enhanced spatial and temporal resolution, is uniquely capable of furthering this line of inquiry by quantitatively incorporating concussive impact, along with concomitant biochemical, morphological, and electrophysiological assessment, simultaneously in the same preparation.

In the current study, using TBI-on-a-chip integrated with computational modeling, we have established a map of differential forces on the network adhered-MEA "chip" using finite element analysis. We found that impacts induced an overall loss of dendritic spines and increased levels of mislocalized tau coupled with acrolein. These impact-induced changes are significantly intensified at the "edges" of the MEA, where the calculated force was higher relative to that at the MEA "center". Inter-

estingly, acrolein exposure in the absence of impact is capable of partially mirroring these impact-induced phenomena. Furthermore, we show that impacts result in a severity-dependent reduction of electrophysiological activity, a deficit that can also be mimicked using acrolein. We also show that relatively high *g*-force (200*g*) impacts significantly alter burst amplitude, an observation that, when combined with our previous electrophysiological study,[8] continues to suggest impact-induced changes in network dynamics. These results reveal the quantitative relationship between mechanical forces and resulting biochemical, structural, and functional injuries, in cultured neuronal networks, with greater spatial and temporal resolution than previously possible. Taken together, this study, along with several previous reports utilizing TBI-on-a-chip, continues to implicate acrolein as a key culprit in both TBI and AD, suggesting that acrolein could provide a promising therapeutic target for slowing or even preventing the progression of TBI to AD.

## Methods

### Primary neuron culture

Neuronal networks were generated utilizing previously established methods.[7–9] Briefly, frontal cortex tissues were harvested from E-16 embryos of ICR mice (Envigo, Inc., 3040F), employing the protocols of Ransom *et al.*[21] with minor modifications.[22–24] Isolated cortices were mechanically separated, enzymatically digested in a 0.05% trypsin solution (Gibco, 25300054), triturated, and combined with either NbActiv4 (Fisher, NB4500) for morphological/immunofluorescence studies, or Dulbecco's modified minimal essential medium (DMEM, HyClone, 11965092) supplemented with 4% fetal bovine serum (Gibco, A5256801) and 5% horse serum (Gibco, 26050070) for electrophysiological studies. Morphological studies and electrophysiological cultures were seeded at 20k and 100k cells per 100 μL droplet (or ~3 k and ~14 k per mm$^2$) respectively, in ~3 mm diameter adhesion islands (the circular area in which cells adhere)[8] on 5 × 5 cm custom microelectrode arrays. Post-seeding, cultures were maintained at 37 °C in a 5 or 10% CO$_2$ atmosphere, with biweekly (Monday/Thursday) media replacement, without fetal bovine serum. This approach provides both high-density "histiotypical" recording networks, or networks composed of neuronal and glial cell types representative of the parent tissue (which is verified by combining histology with the method of isolation),[24,25] and low-density neuronal networks for evaluating dendritic features (*i.e.* spines). All animal procedures were performed in accordance with the Guidelines for Care and Use of Laboratory Animals of Purdue University and approved by the Institutional Animal Care and Use Committee (IACUC) of Purdue University, under institutional protocol 1306999879, as well as the recommendation in the ARRIVE guidelines.

### TBI-on-a-chip *in vitro* model of trauma

The "TBI-on-a-chip" *in vitro* trauma model was utilized for the application of all experimental injuries, as previously described and briefly summarized in Fig. 1, and a picture of the device with phase contrast images of networks pre and post

impact can be found in the SI (Fig. S1).[7–9] In summary, this uniquely modified impact pendulum provides real-time electrophysiological and morphological monitoring of neuronal networks grown on microelectrode arrays during rapid acceleration injury within a clinically relevant range of $g$ forces (30–300$g$). This is accomplished with a stainless-steel "miniature-incubator" design, capable of maintaining life-support parameters (physiological pH, osmolarity, and temperature) while withstanding impact-forces of up to 300$g$. This approach produces biomechanical acceleration forces that stress subcellular mechanisms and cellular components while generating limited cell death and can be used to both investigate network activity immediately before and after impact injuries, and/or morphological/immunocytochemical investigations. Further, the modular design of the impact pendulum allows for the adjustment of both impact accelerations and contact times, allowing investigators to explore a broad range of force-distributions.

## Microelectrode array preparation

Microelectrode arrays (MEAs) were fabricated in-house utilizing previously described methods.[26–28] Briefly, MEAs are square, ~1 mm-thick glass plates consisting of 64 photo-etched, semi-transparent indium-tin oxide microelectrodes (10 × 10 μm, each), forming a 1 mm² central array (Fig. 1). Electrode leads were insulated with methyl-trimethoxysilane resin, laser de-insulated at central electrode termini creating shallow (~2 μm deep) recording craters, and subsequently electro-plated with gold to adjust interface impedances to approximately 0.8 mΩ. Prior to seeding, MEAs were mask-flamed for localized surface activation and sequentially coated with poly-D-lysine and laminin.[29] Said simply, flame activation converts the MEA surface from hydrophobic to hydrophilic (favoring cell adhesion) at the exposed/non-mask covered area, thus restricting cell adhesion only to these pre-selected, activated locations. Briefly, poly-D-lysine (0.1 mg mL$^{-1}$, Sigma-Aldrich, P6407) was added to the MEA and left to incubate at 37 °C overnight. The poly-D-lysine was then removed and rinsed 2× with ultrapure water. Laminin (Sigma-Aldrich, L2020, 1 mg mL$^{-1}$) was diluted in DMEM (0.02–0.04 mg mL$^{-1}$) and added to the adhesion area for ~1 hour prior to cell seeding. Of note, prior to experimentation circular "landmarks" were measured and etched into MEA undersides, which provide an additional verification of proper cell placement during morphological studies. Furthermore, accessory experiments featuring dual networks utilized a set of MEAs similarly etched to define our desired parameters (2 separate circles, Edge and Center), with a corresponding custom stainless-steel mask for flaming.
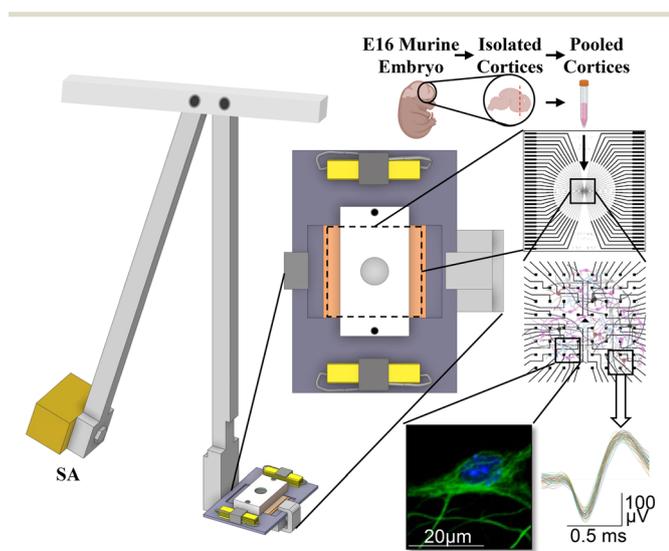


Fig. 1 TBI-on-a-chip injury model overview. The TBI-on-a-chip impact pendulum was utilized to generate rapid acceleration injuries within a clinically relevant range of $g$-forces in neuronal networks grown on optically transparent microelectrode arrays (MEAs). The striker arm (SA) is released from one of several fixed initial-positions, whose forces have been previously established for this model using dual accelerometer measurements that were subsequently verified mathematically for a range between 30 and 300$g$.[8] The force of gravity then guides the SA downward in a pendulous motion to make contact with the target arm and stainless-steel impact-chamber. This airtight "miniature-incubator" system preserves the integrity of the MEA-adhered neuronal network, while maintaining sterility and physiological parameters during injury application and experimentation. To achieve neuronal network formation, E-16 murine frontal cortices are isolated, pooled, mechanically separated and enzymatically digested, before seeding onto custom fabricated MEAs. A corresponding schematic of a typical MEA is also included, exhibiting 32 electrical contacts converging from the left and right edges into a 64-electrode array. Further enlargement reveals a total recording area of 1 × 1 mm², with representative cells. Taken together, this investigative tool offers high-resolution morphological and electrophysiological capabilities. An expanded immunofluorescence image demonstrates the type of optical resolution available in this system. Further, 50 overlapping events from a single, discriminated representative unit during a ~2 hour baseline recording period are included to illustrate unit consistency, indicating the stability of cell-electrode coupling. Dotted line represents zero potential baseline.

## Electrophysiological recording

Network recording experiments were completed using previously described methods.[8,9,28,30] Briefly, neuronal networks (average age: 26 ± 5 days in vitro, a range previously demonstrated to provide intra- and inter-culture reproducibility in this model,[8] and confirmed statistically here to not correlate with treatments (Note S1 and Fig. S2–S5)) cultured on MEAs were aseptically mounted within stainless steel recording chambers that allow the continual maintenance of life-support functions for the duration of the experiments. More specifically, the following were controlled: temperature at 37 °C; a 7.4 pH via continuous flow (10 mL min$^{-1}$) of 10% $CO_2$ in air; and a 300 mOsmol kg$^{-1}$ with ultrapure water infusion.

Analog electrical signals from extracellular spike activity were amplified (10 K total gain) and digitized (40 kHz), before time stamp conversion for storage and post-analysis (Plexon Inc. Multichannel Acquisition Processor System, Dallas TX). Active unit discrimination was accomplished utilizing Plexon's waveshape templates, which provides real-time identification and sorting of individual units. Under optimal

conditions, (visual signal-to-noise ratios >3:1) four separate waveshapes can be distinguished from a single electrode, in real-time. Once templates surpass their respective threshold, the corresponding spikes are logged with a 25 μs sampling resolution.

Whole network activity (spike and burst production) was quantified using previously described methods.[8,22,31,32] Briefly, real-time average network spike production was plotted per minute for the duration of the entire experiment, which served as the primary network activity display. For each minute, total activity was divided by the number of active channels, or channels with at least 10 discriminated spike signals per minute. Burst activity was monitored utilizing the Plexon raster display. Additional spike rate and burst analyses were quantified offline using the NeuroExplorer analysis program (NEX Technologies, Colorado Springs). Burst identification was achieved by integrating time stamps from discriminated waveshape templates with a simulated RC circuit using an integration constant of 70 ms, and applying 2 separate thresholds (T1 and T2). T1 was set at a level close to noise and indicates the potential start of a burst, while T2 was set at a value approximately five times the value of T1 and confirms whether the T1 signal was indeed a burst. Burst termination is influenced by the decay constant, and so a 10 ms adjustment was performed to better match the profile with the concluding spikes for each burst. A 100 ms gap time was used to separate bursts. If the activity remained below T1 for more than 100 ms, then two bursts were generated. This gap time was adjustable, and its selection was dependent on the overall spike patterns observed *via* the time stamp display in NeuroExplorer. For more information about how these burst values are calculated, please see the SI (Note S2). Further, a representative, full-length recording file is currently available in this method's inaugural publication.[8] In summary, while the precise methods of burst identification and pattern feature extraction can vary,[33–36] these descriptions still provide valuable information about network behavior, and can be utilized to reveal major states or modes of the network.[37]

Each network's spontaneous activity is unique, thus data are expressed as percent changes from this network-specific reference activity, which was maintained in its stable state for a minimum of 60 minutes (native activity) wherein activity did not fluctuate greater than ±10% before any experimental manipulation.[8] This native activity exceeded 6 hours in several experiments. All recordings were performed in fresh, standard cell culture media.[8] "Sham" networks were treated identically to impacted networks, with the notable absence of the application of force.

### Computational modeling

A digital twin of the TBI-on-a-chip *in vitro* impact model was used to quantify impact-induced shear stress distributions in MEAs *via* finite element analysis, using a commercially available, industry-standard ANSYS modeling platform (similar to previous multiphysics modeling work performed by this lab).[38,39] The system is comprised of 14 unique parts, summarized in Table 1 and visualized in Fig. 2, which correspond with exact dimensions from the *in vitro* configuration. The computational domain was discretized using unstructured meshing in ANSYS. The glass MEA and rubber O-ring were discretized with a finely resolved mesh at 0.50 mm per grid independence study, while other distant components were more coarsely modeled to increase computational efficiency (Table 1). The model simulates the first 5 ms of impact where the initial time-point represents the moment the striker arm contacts the target arm at a calculable initial velocity that is proportional to the *g*-force. We simulated two cases, with the initial velocity of 1.675 m s$^{-1}$ and 0.827 m s$^{-1}$, corresponding to 200$g$ and 30$g$ impacts, respectively. The numerical solution was obtained in ANSYS Mechanical using the explicit dynamics solver suite with explicit time integration methods to solve the equations of motion. These numerical schemes were specifically used to account for rapidly changing conditions, high speed impacts, and other highly transient physical phenomena. Standard culture medium fluid was best modeled using an Eulerian reference frame with a water

**Table 1** Digital twin parts, materials, and contacts

| Part | Material | Contact type | Mesh size (mm) |
|---|---|---|---|
| Striker arm | STNL.STEEL 2 | Frictional body interaction | 5.0 |
| Target arm | STNL.STEEL 2 | Bonded (to clip) | 5.0 |
| Clip | STNL.STEEL 2 | Bonded (to target arm); bonded (to plate) | 2.0 |
| Plate | STNL.STEEL 2 | Bonded (to clip) | 2.0 |
| Glass MEA | FLOATGLASS | Frictional body interaction | 0.50 |
| Silicone padding | RUBBER1 | Frictional body interaction | 1.0 |
| Rubber O-ring | RUBBER1 | Bonded (to reservoir) | 0.50 |
| Reservoir | STNL.STEEL 2 | Bonded (to rubber O-ring) Bonded (to glass cover) | 2.0 |
| Glass cover | FLOATGLASS | Bonded (to reservoir) | 1.0 |
| Fluid media | WATER2 | Frictional body interaction | 1.0 |
| Screw 1 | STNL.STEEL 2 | Bonded to screw nut 1 | 0.5–1.0 |
| Screw nut 1 | STNL.STEEL 2 | Bonded to screw 1 | 1.0 |
| Screw 2 | STNL.STEEL 2 | Bonded to screw nut 2 | 0.5–1.0 |
| Screw nut 2 | STNL.STEEL 2 | Bonded to screw 2 | 1.0 |
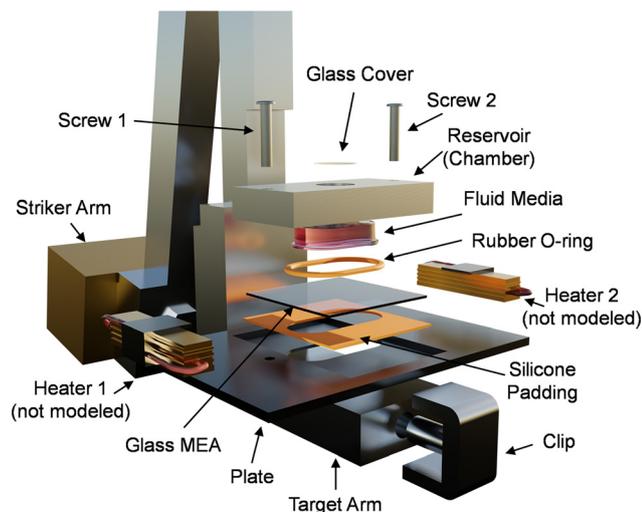
**Fig. 2** Digital twin geometry and boundary conditions. A TBI-on-a-chip "digital twin", or a digital replication of the entire *in vitro* experimental set-up rather than simply the area of interest (MEA), was created using ANSYS SpaceClaim with exact part measurements conducted on the physical model and is shown, deconstructed. The striker arm (SA) and target arm (TA) are affixed at zero-displacement on their inner edge to allow for free-swinging rotation of the arms. SA is given an initial velocity proportional to the *g*-force of the impact, with maximum velocities for 30 and 200*g* experimentally calculated as 0.827 and 1.675 m s$^{-1}$, respectively. Summary information for the parts, materials, and contact types are provided in Methods.

(WATER2) material model which is commonly implemented to model fluid in ANSYS Mechanical. This material model for water has a density of 1000 kg m$^{-3}$ and is described using the Shock EOS linear model with Grüneisen coefficient of 0.28. The rubber O-ring and silicone padding were described using a 3rd order Ogden material type (RUBBER) with material constants as defaulted in the Rubber1 ANSYS Material model. The glass MEA and glass cover slide were modeled as float glass (FLOATGLASS), while all other parts were modeled using the stainless steel (STNL.STEEL 2) material law.

For each time step of the simulation, we computed the components of in-plane shear stress ($\sigma_{yx}$ and $\sigma_{yz}$) on the face of the glass MEA. Time-averaged shear stress (TASS) at each spatial location was calculated as the integral of the shear stress magnitude normalized by the total time duration (eqn (1)). This variable is representative of the amount of time-averaged exposure of cells in a local area to the shear wave propagation through the glass MEA.

$$\text{TASS} = \left( \frac{1}{T} \int_0^T \sqrt{(\sigma_{yx})^2 + (\sigma_{yz})^2} \, dt \right) \quad (1)$$

### Experimental protocols

**Impacts.** TBI-on-a-chip can provide impact injuries throughout a range of clinically relevant *g*-forces, or intensities that best approximate those most likely to appear outside

of the laboratory setting.[7–9] We selected impact forces of 30 and 200*g* (a relatively large force, *i.e.* rapid acceleration/deacceleration injury, like in a motor vehicle accident) to both describe these associated changes as a function of a range of impact forces, while simultaneously highlighting subtle alterations in neuronal networks after mild injury (*i.e.* 30*g*, football heading or mild sports injury), a current issue that still requires much elucidation.[40–42] Network activity was evaluated immediately before and after impact injuries, while morphological evaluations were performed at 24 hours post-impact. All experimental cultures were aged 21 days *in vitro* (D.I.V) unless otherwise noted (see "Electrophysiological recording"), and conducted in tandem with procedurally and age-matched control networks.

**Exogenous acrolein exposure.** In a complimentary group of non-impact experiments, exogenous acrolein was aseptically added to the culture media of neuronal networks, in tandem with procedurally and age-matched controls. An acrolein (Sigma) stock solution (100 mM) was prepared for each experiment, and then diluted with culture media to a final, physiologically-relevant concentration of 100 μM, as previously described.[25,43–46] To best ensure consistency between trials, a new stock solution was made immediately preceding each experiment. This effort is to account for the extremely-reactive nature of acrolein.[46,47] Acrolein-containing culture media were replaced with standard media following a 4 hour exposure period. Network activity was investigated immediately before and after exposure, while morphological analyses were performed at 24 hours post-exposure.

### Viability

Several inaugural studies have established TBI-on-a-chip's ability to consistently produce graded, clinically-relevant impact-injuries with minimal cell-death.[7–9] However, to account for the novel, specific boundaries of this investigation, a complementary viability study was performed, utilizing morphological/immunocytochemical neuronal cultures as described in "Primary neuron culture." Following previously established procedures,[48,49] at 24 hours post-treatment cells were thrice rinsed with isotonic phosphate buffered saline solution (PBS, pH = 7.4, Gibco), exposed to a 25 μM and 7.5 μM concentration of fluorescein diacetate (FDA) and propidium iodide (PI), respectively, for 5 minutes, and then imaged in PBS. Non-impact control networks revealed an average cellular viability of 86.7 ± 1.1%, a value which is comparable to our previously published findings. When compared to networks that experienced the maximum impact forces provided in this study (200*g*), no significant difference was observed (85.5 ± 1.2% viability, *n* = 5, *p* > 0.05).

### Immunofluorescence staining and antibodies

Immunofluorescent staining of neuronal networks was performed as previously described.[7,18,50–54] Briefly, cultures were thrice rinsed with PBS and fixed using 4% paraformaldehyde (Thermo Scientific) at 24 hours post-treatment. Networks

were then washed using PBS, permeabilized with 0.2% Triton (Sigma), blocked with 10% normal donkey serum blocking solution (Abcam, AB7475), and treated overnight with primary antibodies at 4 °C. After primary antibody removal, cells were gently rinsed with 0.01% Tween-20 (Sigma), treated with secondary antibodies (2 hours), and subsequently sealed using ProLong Gold antifade reagent (Fisher, P36930). The following antibodies and stains were utilized in this study: mouse anti-acrolein (Stressmarq, SMC-504D); rabbit anti-Tau (Abcam, ab76128); Phalloidin-iFluor 488 reagent (Abcam, ab176753); rabbit anti-MAP2 (GeneTex, #GTX133109); chicken anti-MAP2 (AvesLabs, #MAP-0020); Alexa Fluor 594 (Jackson Immunoresearch, 715-585-151, 703-585-155, and 711-585-152); Alexa Fluor Plus 405 (Fisher, A48258). Digital imaging was performed with a Zeiss LSM 880 microscope (Carl Zeiss, Germany) using ZEN black software, and 15-image stacks with a 0.36 μm step in the z direction separating each image were acquired. Stack processing and image analysis were performed using ImageJ (NIH). Slices were averaged into a single image, the corresponding channels for each marker of interest were paired and overlaid for analysis, and spine numbers with dendritic lengths were measured utilizing the dendrite spine counter plugin (ImageJ). Dendritic spine densities were analyzed and compared as the number of spines per 100 μm dendrite segment. Quantitative fluorescence measures treated spines as binary events, confirming either the presence or absence of tau or acrolein–Lys adducts.

### Statistical analysis

Unless noted, all analyses were performed as subsequently explained. Immunocytochemical and fluorescence data were analyzed as previously described, with minor modifications[7–9,18,50,55] For this study, quantitative immunofluorescence and morphometrical data for each treatment were reported from sets of 5 MEAs, with average measurements from 2 separate non-overlapping network sections (10 total, per treatment). In other words, a pre-selected area of the MEA, uniform between all treatments, was imaged, and all the neuronal processes in these image frames were analyzed. While this systematic imaging approach reduces potential user bias, it also provides data indiscriminately with regards to the total length of a single process (or how the image-frame dissects processes), thus the results are best described as average spines per fixed length of processes. Dendritic spines were obtained using the dendritic spine counter plugin for ImageJ, which identified features between 1 and 3 μm and utilized a 50% sensitivity. Each identified feature was visually verified and then characterized using the dendritic spine counter. Image average values were used for statistical analysis, which are presented as control-normalized average values. Standard deviations are included to demonstrate the variation between samples.

StataSE16 and Microsoft Excel were used to perform statistical analysis. A one-way analysis of variance (ANOVA) was utilized to establish significance between multiple treatments, with Scheffe *post hoc* analysis. In experimental analyses that only required comparisons between two groups, a Student's *t*-test was used. In all experiments statistical significance was defined as *p* value $<0.05$.

## Results

### The reduction of dendritic spine density, mislocalization of tau, and increase of acrolein, as a function of impact

Immunocytochemical evaluations of neurons from neuronal networks receiving a 200 g impact-injury revealed significant increases of both tau mislocalization and endogenous acrolein (acrolein–Lys adducts) levels in dendritic spines, with reductions in total dendritic spine densities, at 24 hours post-impact (as compared to procedurally and age matched control networks), and were visualized with fluorescence imaging (Fig. 3 and 4). Phalloidin labeling with high-resolution confocal microscopy revealed relatively distinct dendritic protrusions (spines), with tau intermittently presenting as spine-confined globules whose boundaries were slightly retracted from spine perimeters. Acrolein–Lys adducts exhibited similar patterns, while showing a more diffuse distribution
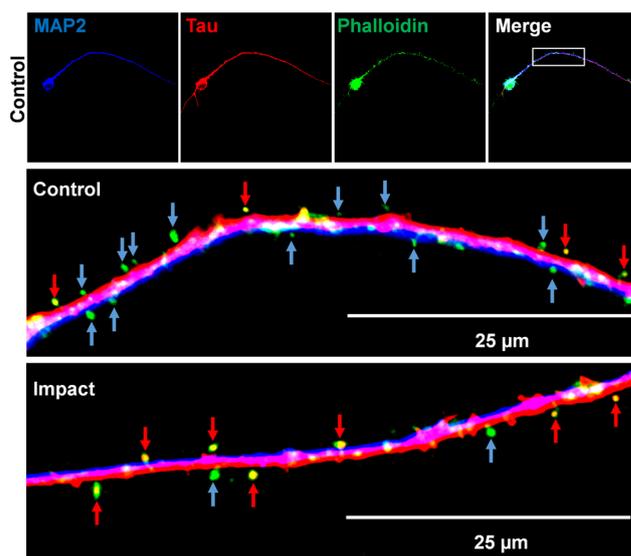


**Fig. 3** Immunocytochemical assessment of increases in tau mislocalization in dendritic spines as a function of impact injury. Representative fluorescence images of neurons from neuronal networks at ×63 magnification for "control" and "impact" (200*g*) treatments, at standard "center" locations (see Fig. 7–10 for introduction, explanation, and use, of "center" *vs.* edge" terminologies). Neuronal features are visualized *via* f-actin using Phalloidin-iFluor 488 (green) from Abcam (ab176753), tau with anti-tau antibody (blue) from Abcam (ab76128), and MAP2 with anti-MAP2 (red) from AvesLabs (#MAP-0020). At this initial resolution, control and impact neurons present similar patterns and levels of tau expression throughout somata and neurites, which can be visualized in context at the corresponding merge series. However, enhanced magnification and examination of dendritic spines reveals distinct differences. By comparing an enlarged section from the control (white box) with an analogous impact section (upper and lower-bottom, respectively) merge series, a change in the overall number of dendritic spines is noted, as illustrated through the use of arrows. Further, there is a significant increase in spines that present with tau (red arrows), as compared to neurons from control networks.
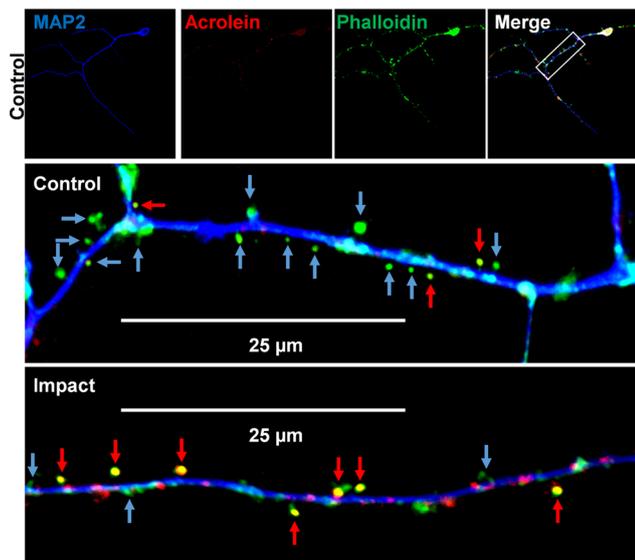
**Fig. 4** Immunocytochemical assessment of increases in acrolein–Lys adducts in dendritic spines as a function of impact injury. Representative fluorescence images of neurons from neuronal networks at ×63 magnification for "control" and "impact" (200$g$) treatments, at standard "center" locations (see Fig. 7–10 for introduction, explanation, and use, of "center" *vs.* edge" terminologies). Neuronal features are visualized *via* f-actin using Phalloidin-iFluor 488 (green) from Abcam (ab176753), acrolein–Lys adducts with anti-acrolein antibody (red) from Stressmarq (SMC-504D), and MAP2 with anti-MAP2 (red) from Genetex (#GTX133109). Consistent with our previous reports, control and impact neurons present with varying levels of acrolein expressed throughout somata and neurites, which is exemplified in the corresponding merge series. Further, upon closer examination of an enlarged section from the control (white box) merge series, the distinct appearance of acrolein–Lys adducts in dendritic spines becomes apparent. Again, a reduction in the total dendritic spine density of neurons from impact networks compared to the control is noted (arrows). Further, the ratio of spines with acrolein present (red arrows) is increased significantly in impact neurons compared to the control.

throughout the spine. These results were quantified as ratios (presence/absence), and presented as average percent control values ± standard deviations (Fig. 5). In summary, neurons from impacted networks showed an average 38 ± 11% reduction in dendritic spine densities, or number of dendritic spines per 100 μm segment of dendrite ($n$ = 10, $p$ < 0.01, when compared to non-impact control networks). Further, the presence of tau and acrolein in impacted dendritic spines increased by 135 ± 34% and 184 ± 71% on average (respectively), when compared to neurons from non-impact control networks ($n$ = 10, $p$ < 0.01, for both).

### The reduction of dendritic spine densities and increase in tau mislocalization as a function of acrolein exposure

To investigate the possible role of acrolein in the impact-induced mislocalization of tau into dendritic spines, exogenous acrolein was added into the media of non-impacted neuronal networks (Fig. 6). Briefly, networks were exposed to acrolein at a 100 μM concentration for a 4 hour period (ACR),

with analysis at 24 hours post-exposure. Interestingly, neurons from acrolein-exposed networks showed average decreases in the number of dendritic spines per 100 μm dendrite-segment of 44 ± 21% ($n$ = 10, $p$ < 0.01, when compared to non-exposed controls). Further, ACR neurons revealed average increases in tau-positive dendritic spines of 175 ± 46%, when compared to non-exposed controls ($n$ = 10, $p$ < 0.01).

### MEA shear stresses as a function of impact force in the TBI-on-a-chip digital twin: center *vs.* edge

Computational modeling of the *in silico* digital twin allowed for estimation of loading on the glass MEA across various $g$-force impacts as well as providing information about the spatial changes within each glass MEA. To quantify the loading experienced across the glass MEA where neurons are seeded, TASS (time averaged shear stress) was used as a metric of the local amount of stress. To account for the disparity between the spatial resolution of the computational model, with an element edge length of 0.50 mm, and the sampling location of the *in vitro* experiments, with a 2.0 mm$^2$ sampling area, 16 elements centered around each location, totaling a 2.0 mm$^2$ area, were averaged to compute the TASS metric. The computational model revealed a significant difference for the TASS experienced at the center of the glass MEA, termed "center", compared to a location adjacent to the reservoir wall on the impact side, termed "edge" (Fig. 7). Significant spatial differences in TASS were observed in both the 30$g$ ($p$ < 0.01) and 200$g$ impacts ($p$ < 0.01), with edge locations experiencing TASS increases of 37 ± 25% and 364 ± 138% in 30$g$ and 200$g$ impacts (respectively), relative to each corresponding center location.

### The reduction of dendritic spine density, mislocalization of tau, and increase of acrolein, as a function of shear stress

To directly investigate cell-scale shear stresses with the associated neuronal changes in the TBI-on-a-chip system, identical cell culture methods were utilized to generate an additional neuronal network on the same MEA at a separate locality expected to experience relatively higher-stresses (edge), subsequently exposed to a 200$g$ impact upon maturation, and analyzed at 24 hours post-injury. The results were compared with our previous, centralized location of predicted relatively lower-stresses (center) (Fig. 8). In summary, while both "edge" and "center" neurons showed significant reductions in the amount of dendritic spines post-impact, edge neurons revealed greater spine losses. Specifically, impacted edge neurons revealed average decreases in the total number of dendritic spines per 100 μm dendrite-segment of 8% more than impacted center neurons ($n$ = 10, $p$ < 0.01). Similarly, the presence of tau and acrolein in impacted edge dendritic spines had a further increase of 59% and 92% on average (respectively), greater than impacted center neurons ($n$ = 10, $p$ < 0.01, for both). As expected, neurons from non-impacted
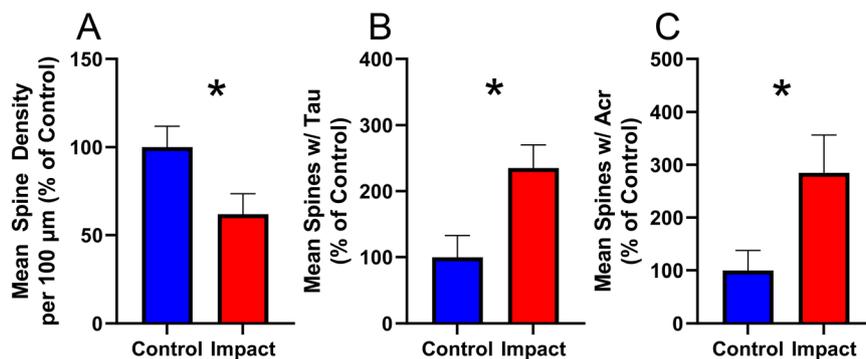
**Fig. 5** Quantification of tau and acrolein–Lys adducts in dendritic spines with dendritic spine densities as a function of impact-injury. Immunocytochemistry (ICC) with immunofluorescence (IF) was utilized to detect and quantify the total density of dendritic spines, in addition to the presence of tau and acrolein–Lys adducts in the dendritic spines, for neurons from neuronal networks at 24 hours post-impact, which are compared to neurons from procedurally and age-matched control networks. (A) Average number of dendritic spines per 100 μm of dendrite segment in neurons from control and impact (200$g$) networks, given as percent control values. Interestingly, impact neurons reveal a significant decrease in average dendritic spine densities compared to neurons from control networks. Further, the remaining spines of impact neurons revealed a significant average increase in the presence of both tau (B) and acrolein–Lys adducts (C) relative to the control (respectively), which are also presented as percent control values. Dendritic spines were quantified, with subsequent acrolein–Lys and tau antibody fluorescence intensities categorically analyzed (presence or absence), using ImageJ (NIH), and are presented as % control values ± SD ($n$ = 10, 2 averages from 5 separate networks). Image frames consisted of an average of 315 ± 71 S.D. μm of total processes from multiple neurons. A Student's $t$-test was used to determine significance: * $p < 0.01$.

control networks revealed no significant differences between center and edge locations.
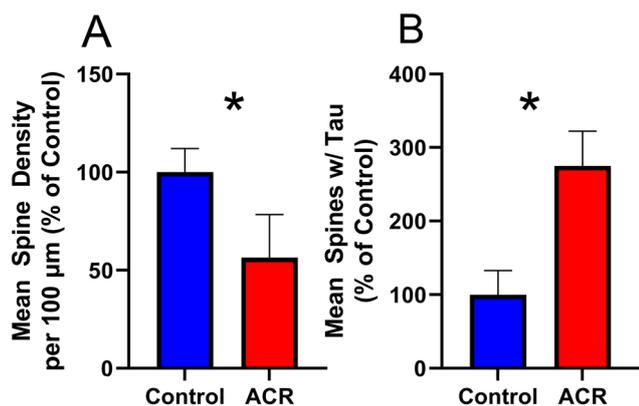


**Fig. 6** Acrolein exposure increases tau mislocalization to dendritic spines and reduces dendritic spine densities. Neuronal networks were exposed to acrolein concentrations of 100 μM for a 4 hour period, and ICC with IF was utilized to detect and quantify the total density of dendritic spines, and the presence of tau in the dendritic spines, at 24 hours post-exposure, which are compared to procedurally and age-matched control networks. Interestingly, (A) neurons exposed to acrolein (ACR) revealed significant decreases in the average number of dendritic spines per 100 μm segment of dendrite compared to neurons from control networks. (B) Further, the remaining spines of ACR neurons show significant average increases in the presence of tau, relative to neurons from control networks. Dendritic spines were quantified, with subsequent tau antibody fluorescence intensities categorically analyzed (presence or absence), using ImageJ (NIH), and are presented as % control values ± SD ($n$ = 10, 2 averages from 5 separate networks). Image frames consisted of an average of 315 ± 71 S.D. μm of total processes from multiple neurons. A Student's $t$-test was used to determine significance: * $p < 0.01$.
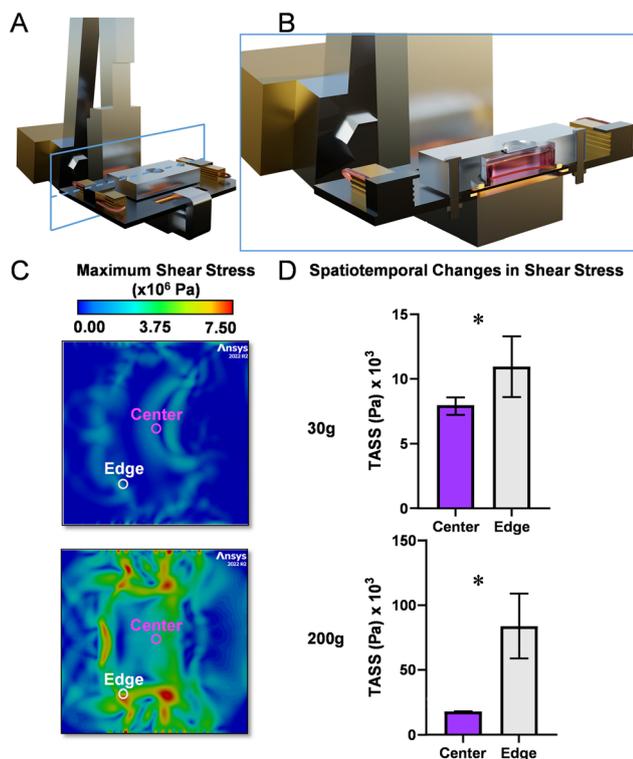
## Impact injury and acrolein exposure cause immediate deficits in network action potential production

The electrophysiological component of the TBI-on-a-chip system was utilized to examine changes of action potential frequencies in histiotypical neuronal networks immediately following sham (networks that were treated identically to impact networks with the notable absence of force-application), impact (30 or 200$g$), or acrolein exposure treatments (Fig. 9). Stable, pre-treatment reference activity was established for a minimum of 1 hour before any experimental manipulation. The stability of cell–electrode coupling was demonstrated by comparing averages of discriminated unit waveshapes for a 20 minute period before (pre, blue) and after treatments (post, red) (Fig. 9A). As shown, post-treatment averaged waveshapes from individual units/neurons showed no significant difference for any treatment ($n$ = 20 waveshapes from individual units/neurons per treatment, $p > 0.05$, compared to each unit's respective pre-treatment waveshape). Overall network activity was described as average spikes per minute (SPM) and normalized to network-specific pre-treatment activity for inter-network comparisons of treatments (Fig. 9B, raw data values can be found in the SI). Examination and comparison of consecutive 20 minute segments of average network activity immediately pre- and post-treatments revealed common attributes of activity reduction relative to pre-treatment reference activity. In summary, impacted-networks (30 and 200$g$) can be described using a 2 plateau response profile during this 20 minute period, with each plateau becoming more pronounced at greater $g$-forces.[8] For example, the network experiencing a 30$g$ impact in Fig. 9B shows an average 10% activity deficit over the 5 minute period post-impact (red line, plateau 1), followed by a

**Fig. 7** Digital twin simulation. Digital replication of the *in vitro* experimental set-up was created using ANSYS SpaceClaim, and then 30$g$ and 200$g$ impacts were simulated using the ANSYS explicit dynamics solver. (A) A more experimentally-relevant depiction of the digital twin geometry (expanded in Fig. 2), with (B) a cross-sectional view, to better contextualize the location of the glass MEA examined in C and D. This digital twin was used to simulate impacts and ultimately guide a finite element analysis of MEA shear stresses, which are visualized in (C) and explained in "Methods". Static time points at 1.83 ms for 30 and 200$g$ impacts reveal spatial variations in maximum shear stress distribution at the "center" (magenta circle) and "edge" (white circle). These key findings are summarized in (D) as the amount of shear stress over the course of the impact, or time-averaged shear stress (TASS), at center and edge spatial locations. The asterisks shown in panel (D) correspond to $p < 0.01$. Note: the pair of resistors used for heating shown in gold and red are not explicitly simulated but were added for visual accuracy of the experimental set-up.

gradual recovery to ~5% of the original reference activity, where it stabilizes (plateau 2). This profile is repeated for 200$g$ impacts, with more prominent reductions in activity for plateau 1 (20%) and plateau 2 (10%). As anticipated, matching sham treatments lacked such features. Interestingly, the addition of 100 μM acrolein generated a rapid (5 min) decline in activity of ~10%, which got progressively worse over the 20 minute observation period. To better examine these inceptive, more distinct 5 minute periods (plateau 1), networks were decomposed into their contributing neuronal units (~20 representative units shown), averaged (SPM), and normalized to each unit's pre-treatment reference activity (Fig. 9C). These changes are statistically described in Fig. 10, but in summary it is clear that the majority of units contribute to this deficit, becoming more distinct with greater $g$ forces and exposure to acrolein. It is interesting to note that

~5% of the total units analyzed showed minor increases in activity following treatment (Fig. 9c arrows). While not statistically significant or large enough to influence the aforementioned network response profiles, this phenomenon was seen in multiple experiments.

### Impact injury and acrolein exposure cause immediate changes in network dynamics

Electrophysiological network recordings were triplicated for each experimental treatment to statistically examine network spike rates (Fig. 10) and activity features during 5 minute periods immediately pre- and post-treatments, using integrated burst activity and spike trains, and action potential frequencies. All results are presented as average activity measures ± standard deviations, and are normalized to network-specific pre-treatment reference activity (raw data values can be found in the SI). Treated networks revealed significant decreases in their average spike rate production as follows: 9.7 ± 4.6% for 30$g$ impacts; 17.3 ± 4.4% for 200$g$ impacts; and 12.7 ± 4.3% for acrolein-exposed networks ($n$ = 3 networks, $p < 0.01$, when compared to each network's respective pre-treatment reference activity) (Fig. 10A). Further, burst rates were also significantly decreased for both 200$g$ impact and acrolein treatments, with average deficits of: 34.4 ± 13.5% for 200$g$ impacts; and 25.8 ± 9.3% for acrolein-exposed networks ($n$ = 3 networks, $p < 0.01$, when compared to each network's respective pre-treatment reference activity) (Fig. 10B). Shams revealed no significant differences between average spike or burst rates ($n$ = 3 networks, $p > 0.05$) (Fig. 10A and B). However, only large impact forces (200$g$) produced significant decreases in burst amplitudes, with an average reduction of 3.51 ± 2.5% ($n$ = 3 networks, $p < 0.01$, compared to pre-treatment reference activity) (Fig. 10C). Sham, 30$g$ impacts, and even acrolein exposure, did not produce significant changes in burst amplitudes ($p > 0.05$).

## Discussion

Using the recently established TBI-on-a-chip system, which emulates concussive injury through a clinically relevant range of impact $g$-forces,[7-9,56,57] we demonstrate that impact injuries produce consistent, measurable alterations in the dendritic spines of murine cortical neuronal networks at 24 hours post-injury. These changes include an increased prevalence of both tau and acrolein, a known mediator of synaptic disruption and demonstrated marker of oxidative stress (respectively),[18,58-61] in impacted dendritic spines, in addition to significant reductions in the total densities of dendritic spines.[62,63] Further, we reveal similar changes in the dendritic spines of non-impacted neuronal networks exposed to a pathologically relevant concentration of exogenous acrolein,[43-46] suggesting that acrolein could play a pivotal role in trauma-induced tau mislocalization and the associated synaptic alterations. To quantitate the relationship between mechanical force and subsequent pathologies, we constructed a digital twin of TBI-on-a-chip to map the distribution of peak shear stresses throughout the MEA during impact-
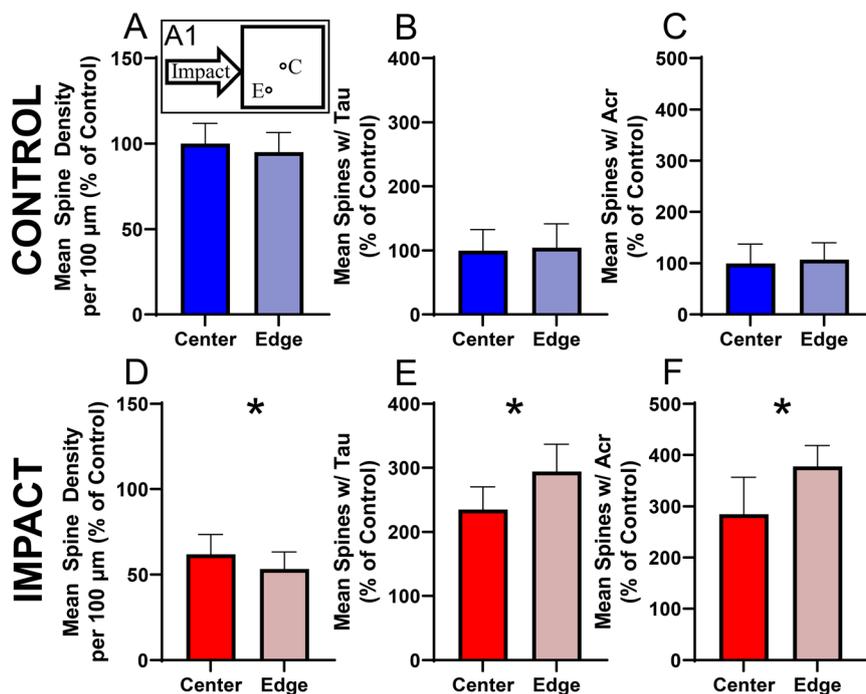
**Fig. 8** Quantifying intra-plate variations of tau and acrolein–Lys adducts in dendritic spines with dendritic spine densities as a function of impact-injury. The TBI-on-a-chip digital twin was utilized to spatially-guide initial culture-seeding during neuronal network generation, to produce a "dual-network" technique (a schematic is provided in A1). This approach features one standard centralized-network (as described in Methods and termed "center," or "C"), and one network that is off-centered ("edge," or "E") at a precise location predicted to experience significantly greater stresses. Again, ICC with IF was utilized to detect and quantify the total density of dendritic spines, in addition to the presence of tau and acrolein–Lys adducts in the dendritic spines, from neurons at center and edge locations at 24 hours post-impact, which are compared to neurons from procedurally, location (center *vs.* edge), and age-matched control networks. As expected, no significant difference was shown between neurons from center and edge locations in control networks for any treatment (A–C). However, neurons from impact-edge networks revealed a minor but significant decrease in average dendritic spine densities compared to impact-center networks (D). Further, the spines of impact-edge neurons revealed a significant average increase in the presence of both tau (E) and acrolein–Lys adducts (F), relative to impact-center networks. Dendritic spines were quantified, with subsequent acrolein–Lys and tau antibody fluorescence intensities categorically analyzed (presence or absence), using ImageJ (NIH), and are presented as % control values ± SD ($n = 10$, 2 averages from 5 separate networks). A Student's *t*-test was used to determine significance: * $p < 0.01$.

events using finite element analysis. This computational modeling based approach provides further evidence linking increasing mechanical forces to greater disruptions in dendritic spines, while also serving to better quantify the impact-generated mechanical stresses in this model. Furthermore, we correlate these impact-induced alterations in dendritic spines with network activity at ultra-acute time points (~3 minutes post-impact) utilizing the electrophysiological component of the TBI-on-a-chip system, revealing almost immediate changes in action potential frequency and burst amplitude, a finding that, in combination with our previous study, 8 strongly suggests changes in network dynamics. Again, many of these associated changes in activity are partially reproduced *via* acrolein exposure in the absence of impact, providing further evidence that acrolein could play a key role in impact induced tauopathies and the accompanying synaptic dysfunctions.

The computational results from finite element analysis of the digital-twin in this report are in good agreement with the experimental data from the TBI-on-a-chip system. In other words, networks at areas of the MEA that were predicted to experience higher stresses, according to the fine element

analysis, showed relatively greater increases of endogenous acrolein production, mislocalized tau, and reductions in spine densities. This combined approach describes cell-scale consequences of macroscale mechanical deformations, and links these numerical results with alterations in neuronal physiology. Specifically, we have shown that increases of TASS are corelated with significant decreases in average dendritic spine densities, and increased levels of both tau and acrolein in dendritic spines. It is important to note that several key simplifications were made in building our finite-element "digital twin." First, the fluid medium is represented in ANSYS Autodyn's structural module using an Eulerian reference (WATER2), rather than through a full Navier–Stokes solution; this approach captures the gross pressure–wave propagation without the detailed velocity field, but is sufficient to reproduce shear-wave transmission accurately for our geometry. Second, our time-averaged shear-stress metric (TASS) is computed from the two in-plane components ($\sigma_{yx}$ and $\sigma_{yz}$) of the mechanical shear wave induced by the pendulum strike; out-of-plane stresses and fluid inertia are therefore neglected. However, we directly validate these simplifications by
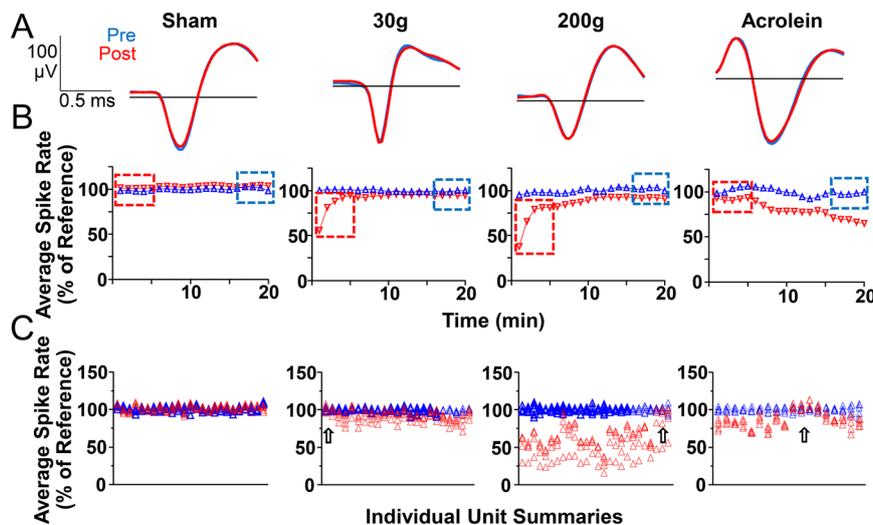
**Fig. 9** Examination of immediate changes in network action potential frequency as a function of impact-injuries and acrolein exposure. Representative electrophysiological response profiles for histiotypical neuronal networks on MEAs immediately before and after sham, 30$g$ or 200$g$ impacts, or exposure to a physiologically relevant concentration of acrolein (100 μM). (A) Waveforms (Plexon, Inc.) from single, representative units, averaged over a 20 minute period immediately before (blue) and after (red) each treatment. No significant difference is shown for any treatment ($p >$ 0.05), indicating the stability of the cell–electrode coupling. Dotted line represents zero potential baseline. (B) Overall network activity shown as average spikes per minute, normalized to network specific pre-treatment reference activity. Consecutive 20 minute segments of normalized average network activity pre (blue) and post (red) each treatment for single, representative networks. Thus, the end ($x$ = 20 min) of the blue line is approximately the beginning ($x$ = 0 min) of the corresponding red line, separated by each respective treatment. As anticipated, sham activities are indistinguishable, with no discernable difference between pre-treatment reference and post-sham segments. However, an ~10% deficit appears after a mild, 30$g$ impact, which gradually (15 minute) recovers to ~5% of the original reference activity. This deficit becomes much more pronounced after a 200$g$ impact, resulting in an initial ~20% activity deficit that stabilizes at ~10% of pre-impact reference activity over a ~15 minute period. Interestingly, acrolein exposure (100 μM) was capable of generating an almost immediate ~10% deficit that advanced over the 20 minute period. Expanded analysis of the corresponding blue and red-boxed 5 minute segments are shown in (C). (C) Average network activity from boxed pre-treatment reference and post-treatment segments for each treatment in (B) are deconstructed into representative subsets (~20 neurons each) of each respective network's comprising units, for the 5 minute periods immediately preceding and following each treatment. Namely, the blue box at the right of each graph represents the activity directly before the treatment, while the red box on the left is the activity immediately following the treatment, and (C) provides a brief overview of the individual units that generate these averages. Average activity for each minute, or 5 blue (pre) and red (post) triangles per neuron/unit (10 total triangles) is shown. While sham networks exhibited minimal variations, deficits in individual unit activity increased significantly in response to impact forces. Similar to network impact responses, acrolein exposure resulted in individual unit deficits located approximately between 30$g$ and 200$g$ treatment deficits. While the scale of the $y$-axes in (B) is consistent to allow for rapid comparison between treatments, it should be emphasized that the reduction in average activity is significantly greater in 200$g$ vs. 30$g$, which is more evident in (C) and statistically demonstrated in Fig. 10. It is also interesting to note that a non-significant number of experimental units revealed minor increases in activity (arrows). In summary, these plots are simply another way to visually illustrate that most neurons participate in these electrophysiological responses rather than outliers influencing the average, a foundational point that has been established in a previous publication but is briefly reiterated here for comprehensiveness.[8] Waveform averages were quantified using Plexon/NeuroExplorer ($n$ = 20, pre- and post-treatment). A Student's $t$-test was used to determine significance: * $p < 0.05$.

comparing the predicted spatial distribution of TASS with the experimentally measured dendritic-spine changes and tau mislocalization (Fig. 7 and 8), which, as expected, reveal significant correlations between elevated stresses and increases in cellular alterations (i.e. "center" vs. "edge"). We therefore conclude that these modeling choices do not materially affect our conclusions about the relationship between mechanical shear and tau pathology."

It is interesting to note that several previous studies have demonstrated neuronal pathological changes at the cellular level in response to mechanical trauma, such as diffuse axonal injuries.[64–66] Further, multiple clinical,[67,68] animal,[67,69] and even some in vitro studies,[18] have strongly suggested a correlation between increasing mechanical forces and pathological alterations of tau. Here, we continue these efforts by presenting and demonstrating an in vitro TBI model of

tauopathy, providing some of the most-direct cellular-evidence linking impact-induced shear stresses to tau abnormalities and oxidative stress, in an impact-dependent fashion. Taken together, these observations continue to suggest that the amount of mechanical stress inputted during neuronal deformation events is directly related to the severity of the resulting tauopathy. Therefore, the enhanced spatial and temporal resolution offered by this model could be key in helping to unveil the biomechanical contributions of TBI towards AD, CTE, and other tauopathies. While these findings serve to contribute to our understanding of the earliest steps of tau mislocalization, a critical step in the pathogenesis of tauopathies such as AD, it is important to reiterate the utilization of wild type mice in the present studies, a factor that must be taken into consideration when drawing conclusions (especially in a non-acute setting). More specifically, wild type
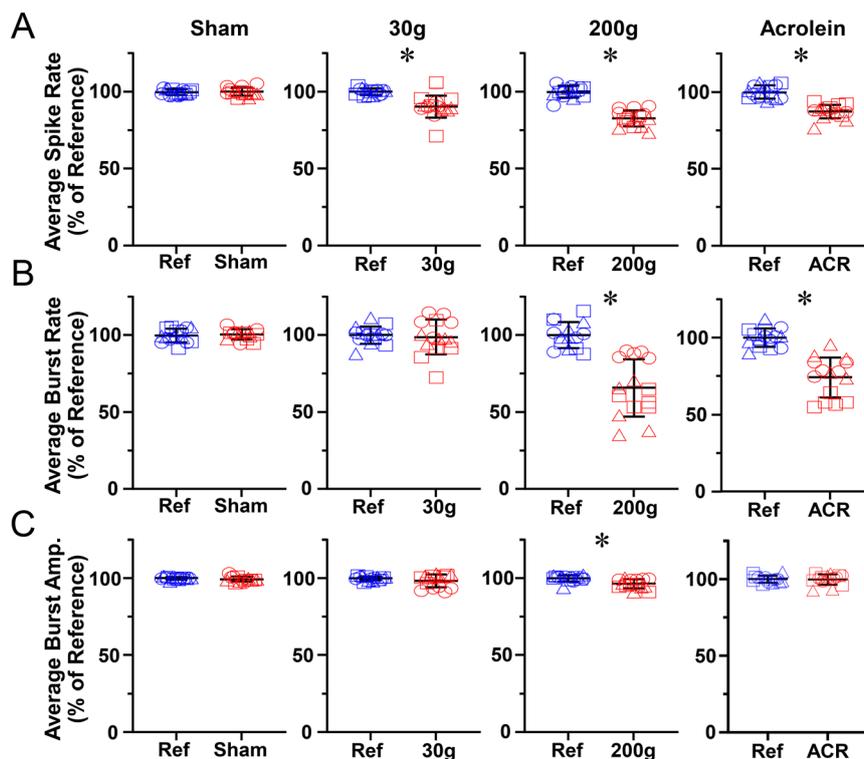
**Fig. 10** Investigation of immediate alterations in network connectivity as a function of impact-injuries and acrolein exposure. Analysis of multi-network spike rates and activity features from integrated burst activity and spike trains generated during 5 minute periods immediately before (blue) and following (red) treatment. Average spike rate, burst rate, and burst amplitude are given for each minute, or 5 blue (pre) and red (post) points per network (10 total). Each treatment group consists of 3 separate networks, which are represented as either triangles, circles, or squares, throughout (top to bottom). All measures are normalized to network specific pre-treatment reference activity. (A) Comparison of average network spike rate plots. As expected, sham produces no discernable difference, while significant decreases appear with as little as 30$g$, becoming much more pronounced after a 200$g$ impact or exposure to acrolein (100 μM). Similar results are revealed in (B), where corresponding average burst rates reveal significant decreases in 200$g$ impacted and acrolein exposed networks (compared to sham). (C) Interestingly, average burst amplitudes did not significantly differ in sham, 30$g$, or acrolein exposed networks, but did reveal significant deficits in response to larger (200$g$) impact forces. Network activities were quantified using Plexon/NeuroExplorer, and are shown as % pre-treatment reference activity values ± SD. A Student's $t$-test was used to determine significance: * $p < 0.01$.

mice lack the capacity to develop the full spectrum of AD seen in humans, with transgenic modifications being necessary to observe certain phenomena (*i.e.* NFT), which still only model particular features of the disease.

TBI-on-a-chip is unique in its ability to provide simultaneous morphological and electrophysiological access to impacted neuronal cells, allowing for examination of electrical activity at both network and neuron scales. These recording methods are highly sensitive, and as a result are excellent tools for examining synaptic changes and network connectivity. However, these approaches can be technically challenging and expensive, and thus are often overlooked in favor of more available staining and imaging methods. Here, we combine these approaches in a unique way, incorporating electrophysiological investigations of altered connectivity after impact injury with histological analyses, utilizing markers such as tau, which has been used to denote synaptic disruption extensively through multiple approaches, including its displacement, phosphorylation, and aggregation.[70,71] More specifically, the mislocalization of tau into dendritic spines has been demonstrated to precede and mediate synaptic dysfunc-

tion.[18,55,61,72,73] In this study, we utilize TBI-on-a-chip to propose both immediate and longer-term (24 hours) impact-induced functional deficits, indirectly using tau displacement, and directly *via* neuronal network recordings. Further, we correlate these findings to increasing acceleration and shear stresses, revealing subtle impact-induced changes at even mild injury levels (30$g$). These findings are well aligned with our previous study, where we established network activity response profiles to impact injuries in a force-dependent manner, using a plateau-based nomenclature system.[8] While we are currently unable to describe the precise mechanisms that generate each plateau, both the initial drop in activity immediately following the impact (plateau 1) and the subsequent activity plateau ~10–20% below reference (plateau 2) (Fig. 9B), it is likely that multiple adaptive mechanisms (*i.e.* changes in long-term depression or potentiation, structural or synaptic plasticity, glial activation, *etc.*) participate. However, it is highly-probable that separate mechanisms dominate different plateaus, which is reflected in their respective average activities. Taken together, these findings further confirm the link between increasing mechanical forces with

synaptic level disruptions and decreasing function.[18] In addition, the current findings also demonstrate the multifaceted investigative capabilities of the TBI-on-a-chip system, which are expected to inspire additional studies into the subcellular mechanisms that underlie and link trauma and neurodegeneration. For example, the enhanced morphological analysis of mechanical trauma induced alterations in neuronal networks is the theme of an upcoming manuscript, which utilizes similar methods in conjunction with synaptic markers such as synaptophysin and PSD-95. However, it is important to note that this investigation was designed to analyze all dendritic spines indiscriminately and, due to the absence of such markers, cannot differentiate between dendritic spine types. Furthermore, while the majority of dendritic spines are associated with synapses, non-synaptic spines do occur, and can be of greater concern with *in vitro* models. This limitation should be taken into account when interpreting the data presented in this manuscript, especially with regards to structural or functional connectivity.

The markers of oxidative stress and post-synaptic dysfunction utilized in this study were selected based on well-established literature.[7,18,58,74–77] While multiple toxic species of aldehydes are known to be elevated after traumatic injury, we selected acrolein to denote oxidative stress because of its greater total production, superior toxicity and reactivity, and its relatively increased levels of neuronal damage as compared to other $\alpha\beta$-unsaturated aldehydes,[78–81] which makes acrolein an ideal tool for approximating overall aldehyde toxicity and oxidative stress. Further, acrolein has already been implicated in TBI,[10,11,82] AD,[83–86] tau phosphorylation,[87,88] and has even been directly linked with increasing mechanical forces in step-wise, force dependent manner using this model.[7] Furthermore, multiple studies have established acrolein as a disruptor of electrophysiological activity in nerve cell networks.[89–91] Last, AD is characterized by the presence of neurofibrillary tangles (NFT) in the brain, which are accumulations of pathological forms of tau protein.[92–94] Thus, several preceding steps in this pathway (*e.g.* tau hyperphosphorylation, mislocalization, and aggregation) are strongly-hypothesized to be early events in AD pathogenesis.[61] Interestingly, recent clinical studies have revealed abnormal tau activities in the frontal cortices of patients isolated during AD stages I–III, or before the appearance of NFTs.[95,96] Further, many of these pathological associated changes in tau have also been recapitulated in animal models of trauma[97,98] and even identified in the cortex of TBI patients post-injury,[99,100] the corresponding brain region featured in the current investigation. Furthermore, tau aberrations have already been linked to significant alterations in neuronal communication in both TBI[101,102] and AD,[61,72] with one *in vitro* model of stretch injury inducing not only the mislocalization of tau, but also correlating this observation with synaptic disruptions electrophysiologically.[18] In response, we selected tau as our marker for monitoring TBI and AD pathologies.

In previous reports we have demonstrated increased levels of oxidative stress *via* acrolein in the soma and processes of impacted neurons and glia (histiotypical cultures), in a force-dependent fashion at 24 hours post-injury.[7,9] In this investigation, we further resolve this spatial relationship to now reveal the increased presence of acrolein in the dendritic spines of impacted neurons. Interestingly, recent studies have linked increases of oxidative stress with the hyperphosphorylation of tau.[103] Such investigations also reveal that tau phosphorylation can induce relocalization from primarily axonal compartments into somatodendritic compartments, and more specifically dendritic spines.[55,61,72] Further, additional studies have suggested that the modification of several lysine residues inside the microtubule binding region of tau promotes separation and pathological tau aggregation,[104–106] indicating that lysine is likely critical for tau's structural stability. Furthermore, acrolein is an electrophile that is known to preferentially form adducts with lysine (a nucleophile).[107] As such, it is possible that acrolein could disrupt these principal lysine residues, instigating structural instability, separation, and eventual aggregation of tau. Taken together, these data suggest that acrolein could play an important role in these force-induced disturbances of tau, and subsequent synaptic abnormalities.

In this report we show that mislocalized tau is accompanied by increased levels of acrolein in dendritic spines at 24 hours post-impact, but have not yet resolved the absolute origins of these elevations. Therefore, it is possible that predominantly soma-localized acrolein either originates in or diffuses into corresponding axons, participating in the disruption of axon-homeostasis and axoplasmic transport, accelerating or even accompanying the movement of tau into ultimately dendritic spines. However, based on the data from this study we can draw several conclusions. Foremost, because these increased levels of tau mislocalization and reductions of dendritic spine densities can be recreated with the addition of exogenous acrolein alone (in the absence of impact), it is possible that acrolein is involved in this trauma-mediated pathway and the associated synaptic alterations, regardless of its precise, originating subcellular distribution. This notion is further confirmed by the alterations in network activity produced by exposure to exogenous acrolein. In addition, acrolein-scavenging has been shown to significantly mitigate deficits in network activity after exposure to post-impact "conditioned media", known to contain elevated levels of acrolein.[9] Taken together, acrolein scavenging could present a viable method for reducing, or possibly preventing some earlier steps of impact-induced tauopathies, and even provide new opportunities for potential oxidative-stress focused therapeutics.

In summary, this study further confirms the investigative capabilities of our TBI-on-a-chip system for cellular and subcellular investigations. In addition, we utilize aberrations in tau to further validate both the connection between trauma and neurodegeneration, and our ability to accurately recapitulate this phenomenon with our *in vitro* model. Furthermore, we show for the first time that these deficits are accompanied by, and recreated with, acrolein, an alleged key player of secondary injuries in TBI,[7,91] and demonstrated to be a cofactor in AD and tauopathies,[108] signaling a potentially novel approach for

therapeutic interventions. In addition, we elaborate on our previously established impact-injury activity profiles and further resolve immediate, impact-induced changes in action potential production, burst rate, and burst amplitude, providing additional[8] evidence suggesting significant alterations in network dynamics post-impact. These changes are further validated by an accompanying impact-induced reduction of dendritic spines. Finally, through computational modeling we more directly link increasing shear stresses with elevated tau displacement at acute timepoints, an event that has been intensively hypothesized but currently has limited direct support.[18,75] In conclusion, we believe that this and similar *in vitro* approaches could be critical towards offering unique insights into not only the mechanisms that underlie trauma and neurodegeneration, but also in investigating diagnoses and treatment strategies to address both TBI and AD, two crippling conditions currently lacking effective treatments.[109–112]

## Author contributions

Conceptualization: EAR, TCD, VR, RS. Methodology: EAR. Investigation: EAR, TCD, TB, JM, SJM, DK, NK, VR, RS. Supervision: EAR, TCD, VR, RS. Writing – original draft: EAR, TCD, VR, RS. Writing – review & editing: EAR, TCD, TB, JM, SJM, DK, NK, VR, RS.

## Conflicts of interest

The corresponding author Riyi Shi is the co-founder of Neuro Vigor, a start-up company with business interests of developing effective therapies for CNS neurodegenerative diseases and trauma. There are no conflicts of interest for the remaining authors.

## Data availability

All data supporting the findings of this study are included within the manuscript. Supplementary information, including enhanced descriptions of burst identification and raw data values, is available. See **https://doi.org/10.1039/D5LC00067J**.

## Acknowledgements

## References

1 B. Roozenbeek, A. I. Maas and D. K. Menon, Changing patterns in the epidemiology of traumatic brain injury, *Nat. Rev. Neurol.*, 2013, **9**(4), 231–236.

2 J. A. Langlois, W. Rutland-Brown and M. M. Wald, The epidemiology and impact of traumatic brain injury: a brief overview, *J. Head Trauma Rehabil.*, 2006, **21**(5), 375–378.

3 A. J. Hicks, A. C. James, G. Spitz and J. L. Ponsford, Traumatic Brain Injury as a Risk Factor for Dementia and Alzheimer Disease: Critical Review of Study Methodologies, *J. Neurotrauma*, 2019, **36**(23), 3191–3219.

4 A. Walker, B. Chapin, J. Abisambra and S. T. DeKosky, Association between single moderate to severe traumatic brain injury and long-term tauopathy in humans and pre-clinical animal models: a systematic narrative review of the literature, *Acta Neuropathol. Commun.*, 2022, **10**(1), 13.

5 J. Cassidy, L. Carroll, P. Peloso, J. Borg, H. von Holst and L. Holm, Incidence, risk factors and prevention of mild traumatic brain injury: results of the WHO Collaborating Centre Task Force on Mild Traumatic Brain Injury, *J. Rehabil. Med.*, 2004, **43**(Suppl), 28–60.

6 A. Kumar and D. J. Loane, Neuroinflammation after traumatic brain injury: opportunities for therapeutic intervention, *Brain, Behav., Immun.*, 2012, **26**(8), 1191–1201.

7 E. A. Rogers, T. Beauclair, A. Thyen and R. Shi, Utilizing novel TBI-on-a-chip device to link physical impacts to neurodegeneration and decipher primary and secondary injury mechanisms, *Sci. Rep.*, 2022, **12**(1), 11838.

8 E. A. Rogers and G. W. Gross, Simultaneous electrophysiological and morphological assessment of functional damage to neural networks in vitro after 30-300 g impacts, *Sci. Rep.*, 2019, **9**(1), 14994.

9 E. A. Rogers, T. Beauclair, J. Martinez, S. J. Mufti, D. Kim and S. Sun, *et al.*, The contribution of initial concussive forces and resulting acrolein surge to β-amyloid accumulation and functional alterations in neuronal networks using a TBI-on-a-chip model, *Lab Chip*, 2023, **23**(15), 3388–3404.

10 M. K. Walls, N. Race, L. Zheng, S. M. Vega-Alvarez, G. Acosta and J. Park, *et al.*, Structural and biochemical abnormalities in the absence of acute deficits in mild primary blast-induced head trauma, *J. Neurosurg.*, 2016, **124**(3), 675–686.

11 G. Acosta, N. Race, S. Herr, J. Fernandez, J. Tang and E. Rogers, *et al.*, Acrolein-mediated alpha-synuclein pathology involvement in the early post-injury pathogenesis of mild blast-induced Parkinsonian neurodegeneration, *Mol. Cell. Neurosci.*, 2019, **98**, 140–154.

12 U. Sehar, P. Rawat, A. P. Reddy, J. Kopel and P. H. Reddy, Amyloid Beta in Aging and Alzheimer's Disease, *Int. J. Mol. Sci.*, 2022, **23**(21), 12924.

13 J. Ye, H. Wan, S. Chen and G. P. Liu, Targeting tau in Alzheimer's disease: from mechanisms to clinical therapy, *Neural Regener. Res.*, 2024, **19**(7), 1489–1498.

14 C. Ji and E. M. Sigurdsson, Current Status of Clinical Trials on Tau Immunotherapies, *Drugs*, 2021, **81**(10), 1135–1152.

15 F. P. Chong, K. Y. Ng, R. Y. Koh and S. M. Chye, Tau Proteins and Tauopathies in Alzheimer's Disease, *Cell. Mol. Neurobiol.*, 2018, **38**(5), 965–980.

16 A. Katsumoto, H. Takeuchi and F. Tanaka, Tau Pathology in Chronic Traumatic Encephalopathy and Alzheimer's Disease: Similarities and Differences, *Front. Neurol.*, 2019, **10**, 980.

17 Y. Yoshiyama, M. Higuchi, B. Zhang, S. M. Huang, N. Iwata and T. C. Saido, *et al.*, Synapse loss and microglial activation precede tangles in a P301S tauopathy mouse model, *Neuron*, 2007, **53**(3), 337–351.

18 N. J. Braun, K. R. Yao, P. W. Alford and D. Liao, Mechanical injuries of neurons induce tau mislocalization to dendritic spines and tau-dependent synaptic dysfunction, *Proc. Natl. Acad. Sci. U. S. A.*, 2020, **117**(46), 29069–29079.

19 M. Cruz-Haces, J. Tang, G. Acosta, J. Fernandez and R. Shi, Pathological correlations between traumatic brain injury and chronic neurodegenerative diseases, *Transl. Neurodegener.*, 2017, **6**, 20.

20 T. J. Orr, E. Lesha, A. H. Kramer, A. Cecia, J. E. Dugan and B. Schwartz, *et al.*, Traumatic Brain Injury: A Comprehensive Review of Biomechanics and Molecular Pathophysiology, *World Neurosurg.*, 2024, **185**, 74–88.

21 B. R. Ransom, E. Neale, M. Henkart, P. N. Bullock and P. G. Nelson, Mouse spinal cord in cell culture. I. Morphology and intrinsic neuronal electrophysiologic properties, *J. Neurophysiol.*, 1977, **40**(5), 1132–1150.

22 E. W. Keefer, A. Gramowski and G. W. Gross, NMDA receptor-dependent periodic oscillations in cultured spinal cord networks, *J. Neurophysiol.*, 2001, **86**(6), 3030–3042.

23 G. J. Brewer, M. D. Boehler, T. T. Jones and B. C. Wheeler, NbActiv4 medium improvement to Neurobasal/B27 increases neuron synapse densities and network spike rates on multielectrode arrays, *J. Neurosci. Methods*, 2008, **170**(2), 181–187.

24 G. W. Gross and K. V. Gopal, Emerging Histiotypic Properties of Cultured Neuronal Networks, in *Advances in Network Electrophysiology: Using Multi-Electrode Arrays*, ed. M. Taketani and M. Baudry, Springer US, Boston, MA, 2006, pp. 193–214.

25 W. Guenter, J. J. P. Gross and K. Gopal, High Information Content Physiological Biosensors: Nerve cell networks on microelectrode arrays, in *Smart Biosensor Technology*, ed. K. George and A. S. B. Knopf, Taylor and Francis Publishers, 2nd edn, 2019.

26 G. Gross, Multielectrode arrays, *Scholarpedia*, 2011, **6**, 5749.

27 G. W. Gross, W. Y. Wen and J. W. Lin, Transparent indium-tin oxide electrode patterns for extracellular, multisite recording in neuronal cultures, *J. Neurosci. Methods*, 1985, **15**(3), 243–252.

28 G. W. Gross and F. U. Schwalm, A closed flow chamber for long-term multichannel recording and optical monitoring, *J. Neurosci. Methods*, 1994, **52**(1), 73–85.

29 J. H. Lucas, L. E. Czisny and G. W. Gross, Adhesion of cultured mammalian central nervous system neurons to flame-modified hydrophobic surfaces, *In Vitro Cell. Dev. Biol.*, 1986, **22**(1), 37–43.

30 G. W. Gross, B. K. Rhoades, H. M. Azzazy and M. C. Wu, The use of neuronal networks on multielectrode arrays as biosensors, *Biosens. Bioelectron.*, 1995, **10**(6–7), 553–567.

31 S. I. Morefield, E. W. Keefer, K. D. Chapman and G. W. Gross, Drug evaluations using neuronal networks cultured on microelectrode arrays, *Biosens. Bioelectron.*, 2000, **15**(7–8), 383–396.

32 A. Gramowski, K. Jügelt, D. G. Weiss and G. W. Gross, Substance identification by quantitative characterization of oscillatory activity in murine spinal cord networks on microelectrode arrays, *Eur. J. Neurosci.*, 2004, **19**(10), 2815–2825.

33 R. Eckmiller, S. M. Blair and G. Westheimer, Fine structure of saccade bursts in macaque pontine neurons, *Brain Res.*, 1980, **181**(2), 460–464.

34 J. H. Cocatre-Zilgien and F. Delcomyn, Identification of bursts in spike trains, *J. Neurosci. Methods*, 1992, **41**(1), 19–30.

35 E. Cotterill and S. J. Eglen, Burst Detection Methods, *Adv Neurobiol.*, 2019, **22**, 185–206.

36 D. J. Bakkum, M. Radivojevic, U. Frey, F. Franke, A. Hierlemann and H. Takahashi, Parameters for burst detection, *Front. Comput. Neurosci.*, 2013, **7**, 193.

37 G. Gross, *Enabling Technologies for Cultured Neural Networks*, Academic, San Diego, 1994.

38 L. Boussel, V. Rayz, C. McCulloch, A. Martin, G. Acevedo-Bolton and M. Lawton, *et al.*, Aneurysm growth occurs at region of low wall shear stress: patient-specific correlation of hemodynamics and growth in a longitudinal study, *Stroke.*, 2008, **39**(11), 2997–3002.

39 L. Boussel, V. Rayz, A. Martin, G. Acevedo-Bolton, M. T. Lawton and R. Higashida, *et al.*, Phase-contrast magnetic resonance imaging measurements in intracranial aneurysms in vivo of flow patterns, velocity fields, and wall shear stress: comparison with computational fluid dynamics, *Magn. Reson. Med.*, 2009, **61**(2), 409–417.

40 C. Beppi, M. Penner, D. Straumann and S. Y. Bögli, A non-invasive biomechanical model of mild TBI in larval zebrafish, *PLoS One*, 2022, **17**(5), e0268901.

41 Prevention NCfI, *Control. Report to Congress on mild traumatic brain injury in the United States: steps to prevent a serious public health problem: Centers for Disease Control and Prevention*, 2003.

42 D. H. Salat, M. E. Robinson, D. R. Miller, D. C. Clark and R. E. McGlinchey, Neuroimaging of deployment-associated traumatic brain injury (TBI) with a focus on mild TBI (mTBI) since 2009, *Brain Inj.*, 2017, **31**(9), 1204–1219.

43 P. Liu-Snyder, M. P. Logan, R. Shi, D. T. Smith and R. B. Borgens, Neuroprotection from secondary injury by polyethylene glycol requires its internalization, *J. Exp. Biol.*, 2007, **210**(Pt 8), 1455–1462.

44 K. Satoh, S. Yamada, Y. Koike, Y. Igarashi, S. Toyokuni and T. Kumano, *et al.*, A 1-hour enzyme-linked immunosorbent assay for quantitation of acrolein- and hydroxynonenal-modified proteins by epitope-bound casein matrix method, *Anal. Biochem.*, 1999, **270**(2), 323–328.

45 J. P. Eiserich, A. van der Vliet, G. J. Handelman, B. Halliwell and C. E. Cross, Dietary antioxidants and cigarette smoke-induced biomolecular damage: a complex interaction, *Am. J. Clin. Nutr.*, 1995, **62**(6 Suppl), 1490s–1500s.

46 P. Liu-Snyder, H. McNally, R. Shi and R. B. Borgens, Acrolein-mediated mechanisms of neuronal death, *J. Neurosci. Res.*, 2006, **84**(1), 209–218.

47 D. P. Ghilarducci and R. S. Tjeerdema, Fate and effects of acrolein, *Rev. Environ. Contam. Toxicol.*, 1995, **144**, 95–146.

48 L. Jiajia, M. Shinghung, Z. Jiacheng, W. Jialing, X. Dilin and H. Shengquan, *et al.*, Assessment of Neuronal Viability Using Fluorescein Diacetate-Propidium Iodide Double Staining in Cerebellar Granule Neuron Culture, *J. Visualized Exp.*, 2017, **123**, e55442.

49 K. H. Jones and J. A. Senft, An improved method to determine cell viability by simultaneous staining with fluorescein diacetate-propidium iodide, *J. Histochem. Cytochem.*, 1985, **33**(1), 77–79.

50 J. Situ, X. Huang, M. Zuo, Y. Huang, B. Ren and Q. Liu, Comparative Proteomic Analysis Reveals the Effect of Selenoprotein W Deficiency on Oligodendrogenesis in Fear Memory, *Antioxidants*, 2022, **11**(5), 999.

51 B. Igor and W. B. Buchwalow, *Immunohistochemistry: Basics and Methods*, Springer-Verlag, Berlin, Heidelberg, 1st edn, 2010.

52 A. Ambaw, L. Zheng, M. A. Tambe, K. E. Strathearn, G. Acosta and S. A. Hubers, *et al.*, Acrolein-mediated neuronal cell death and alpha-synuclein aggregation: Implications for Parkinson's disease, *Mol. Cell. Neurosci.*, 2018, **88**, 70–82.

53 R. S. Chaves, T. Q. Melo, S. A. Martins and M. F. Ferrari, Protein aggregation containing β-amyloid, α-synuclein and hyperphosphorylated τ in cultured cells of hippocampus, substantia nigra and locus coeruleus after rotenone exposure, *BMC Neurosci.*, 2010, **11**, 144.

54 A. Kremer, H. Maurin, D. Demedts, H. Devijver, P. Borghgraef and F. Van Leuven, Early improved and late defective cognition is reflected by dendritic spines in Tau. P301L mice, *J Neurosci.*, 2011, **31**(49), 18036–18047.

55 B. R. Hoover, M. N. Reed, J. Su, R. D. Penrod, L. A. Kotilinek and M. K. Grant, *et al.*, Tau mislocalization to dendritic spines mediates synaptic dysfunction independently of neurodegeneration, *Neuron*, 2010, **68**(6), 1067–1081.

56 R. S. Naunheim, J. Standeven, C. Richter and L. M. Lewis, Comparison of impact data in hockey, football, and soccer, *J. Trauma*, 2000, **48**(5), 938–941.

57 S. M. Duma, S. J. Manoogian, W. R. Bussone, P. G. Brolinson, M. W. Goforth and J. J. Donnenwerth, *et al.*, Analysis of real-time head accelerations in collegiate football players, *Clin. J. Sport Med.*, 2005, **15**(1), 3–8.

58 J. Park, B. Muratori and R. Shi, Acrolein as a novel therapeutic target for motor and sensory deficits in spinal cord injury, *Neural Regener. Res.*, 2014, **9**(7), 677–683.

59 R. Shi, J. C. Page and M. Tully, Molecular mechanisms of acrolein-mediated myelin destruction in CNS trauma and disease, *Free Radical Res.*, 2015, **49**(7), 888–895.

60 Z. Jia, H. Zhu, J. Li, X. Wang, H. Misra and Y. Li, Oxidative stress in spinal cord injury and antioxidant-based intervention, *Spinal Cord*, 2012, **50**(4), 264–274.

61 P. J. Teravskis, B. R. Oxnard, E. C. Miller, L. Kemper, K. H. Ashe and D. Liao, Phosphorylation in two discrete tau domains regulates a stepwise process leading to postsynaptic dysfunction, *J. Physiol.*, 2021, **599**(9), 2483–2498.

62 M. M. Dorostkar, C. Zou, L. Blazquez-Llorca and J. Herms, Analyzing dendritic spine pathology in Alzheimer's disease: problems and opportunities, *Acta Neuropathol.*, 2015, **130**(1), 1–19.

63 J. N. Campbell, D. Register and S. B. Churn, Traumatic brain injury causes an FK506-sensitive loss and an over-growth of dendritic spines in rat forebrain, *J. Neurotrauma*, 2012, **29**(2), 201–217.

64 R. H. Garman, L. W. Jenkins, R. C. Switzer 3rd, R. A. Bauman, L. C. Tong and P. V. Swauger, *et al.*, Blast exposure in rats with body shielding is characterized primarily by diffuse axonal injury, *J. Neurotrauma*, 2011, **28**(6), 947–959.

65 Y. Li, C. Li, C. Gan, K. Zhao, J. Chen and J. Song, *et al.*, A Precise, Controllable in vitro Model for Diffuse Axonal Injury Through Uniaxial Stretch Injury, *Front. Neurosci.*, 2019, **13**, 1063.

66 A. Yaghmai and J. Povlishock, Traumatically induced reactive change as visualized through the use of monoclonal antibodies targeted to neurofilament subunits, *J. Neuropathol. Exp. Neurol.*, 1992, **51**(2), 158–176.

67 M. K. Shin, E. Vázquez-Rosa, Y. Koh, M. Dhar, K. Chaubey and C. J. Cintrón-Pérez, *et al.*, Reducing acetylated tau is neuroprotective in brain injury, *Cell*, 2021, **184**(10), 2715–2732.e23.

68 M. T. Caprelli, A. J. Mothe and C. H. Tator, CNS Injury: Posttranslational Modification of the Tau Protein as a Biomarker, *Neuroscientist.*, 2019, **25**(1), 8–21.

69 G. Edwards 3rd, J. Zhao, P. K. Dash, C. Soto and I. Moreno-Gonzalez, Traumatic Brain Injury Induces Tau Aggregation and Spreading, *J. Neurotrauma*, 2020, **37**(1), 80–92.

70 E. Hill, T. K. Karikari, K. G. Moffat, M. J. Richardson and M. J. Wall, Introduction of tau oligomers into cortical neurons alters action potential dynamics and disrupts synaptic transmission and plasticity, *eNeuro*, 2019, **6**(5), ENEURO.0166-19.2019.

71 M. Wu, M. Zhang, X. Yin, K. Chen, Z. Hu and Q. Zhou, *et al.*, The role of pathological tau in synaptic dysfunction in Alzheimer's diseases, *Transl. Neurodegener.*, 2021, **10**(1), 45.

72 E. C. Miller, P. J. Teravskis, B. W. Dummer, X. Zhao, R. L. Huganir and D. Liao, Tau phosphorylation and tau mislocalization mediate soluble Aβ oligomer-induced AMPA glutamate receptor signaling deficits, *Eur. J. Neurosci.*, 2014, **39**(7), 1214–1224.

73 D. Liao, E. C. Miller and P. J. Teravskis, Tau acts as a mediator for Alzheimer's disease-related synaptic deficits, *Eur. J. Neurosci.*, 2014, **39**(7), 1202–1213.

74 K. Hamann, A. Durkes, H. Ouyang, K. Uchida, A. Pond and R. Shi, Critical role of acrolein in secondary injury following ex vivo spinal cord trauma, *J. Neurochem.*, 2008, **107**(3), 712–721.

75 N. J. Braun, D. Liao and P. W. Alford, Orientation of neurites influences severity of mechanically induced tau pathology, *Biophys. J.*, 2021, **120**(16), 3272–3282.

76 L. Shi, Y. Lin, Y. Jiao, S. A. Herr, J. Tang and E. Rogers, *et al.*, Acrolein scavenger dimercaprol offers neuroprotection in an animal model of Parkinson's disease: implication of acrolein and TRPA1, *Transl. Neurodegener.*, 2021, **10**(1), 13.

77 L. Shi, C. Huang, Q. Luo, E. Rogers, Y. Xia and W. Liu, *et al.*, The Association of Iron and the Pathologies of Parkinson's Diseases in MPTP/MPP(+)-Induced Neuronal Degeneration in Non-human Primates and in Cell Culture, *Front. Aging Neurosci.*, 2019, **11**, 215.

78 R. Shi, T. Rickett and W. Sun, Acrolein-mediated injury in nervous system trauma and diseases, *Mol. Nutr. Food Res.*, 2011, **55**(9), 1320–1331.

79 H. Esterbauer, R. J. Schaur and H. Zollner, Chemistry and biochemistry of 4-hydroxynonenal, malonaldehyde and related aldehydes, *Free Radical Biol. Med.*, 1991, **11**(1), 81–128.

80 J. F. Stevens and C. S. Maier, Acrolein: sources, metabolism, and biomolecular interactions relevant to human health and disease, *Mol. Nutr. Food Res.*, 2008, **52**(1), 7–25.

81 J. Luo, K. Uchida and R. Shi, Accumulation of acrolein-protein adducts after traumatic spinal cord injury, *Neurochem. Res.*, 2005, **30**(3), 291–295.

82 L. Zheng, J. Park, M. Walls, M. Tully, A. Jannasch and B. Cooper, *et al.*, Determination of urine 3-HPMA, a stable acrolein metabolite in a rat model of spinal cord injury, *J Neurotrauma*, 2013, **30**(15), 1334–1341.

83 M. Singh, T. N. Dang, M. Arseneault and C. Ramassamy, Role of by-products of lipid oxidation in Alzheimer's disease brain: a focus on acrolein, *J. Alzheimer's Dis.*, 2010, **21**(3), 741–756.

84 N. Y. Calingasan, K. Uchida and G. E. Gibson, Protein-bound acrolein: a novel marker of oxidative stress in Alzheimer's disease, *J. Neurochem.*, 1999, **72**(2), 751–756.

85 T. I. Williams, B. C. Lynn, W. R. Markesbery and M. A. Lovell, Increased levels of 4-hydroxynonenal and acrolein, neurotoxic markers of lipid peroxidation, in the brain in Mild Cognitive Impairment and early Alzheimer's disease, *Neurobiol. Aging*, 2006, **27**(8), 1094–1099.

86 C. Chen, J. Lu, W. Peng, M. S. Mak, Y. Yang and Z. Zhu, *et al.*, Acrolein, an endogenous aldehyde induces Alzheimer's disease-like pathologies in mice: A new sporadic AD animal model, *Pharmacol. Res.*, 2022, **175**, 106003.

87 S. M. Alavi Naini and N. Soussi-Yanicostas, Tau Hyperphosphorylation and Oxidative Stress, a Critical Vicious Circle in Neurodegenerative Tauopathies?, *Oxid. Med. Cell. Longevity*, 2015, **2015**, 151979.

88 A. Gómez-Ramos, J. Díaz-Nido, M. A. Smith, G. Perry and J. Avila, Effect of the lipid peroxidation product acrolein on tau phosphorylation in neural cells, *J. Neurosci. Res.*, 2003, **71**(6), 863–870.

89 R. Yan, J. C. Page and R. Shi, Acrolein-mediated conduction loss is partially restored by K$^+$ channel blockers, *J. Neurophysiol.*, 2016, **115**(2), 701–710.

90 Y. Shi, W. Sun, J. J. McBride, J. X. Cheng and R. Shi, Acrolein induces myelin damage in mammalian spinal cord, *J. Neurochem.*, 2011, **117**(3), 554–564.

91 K. Hamann, G. Nehrt, H. Ouyang, B. Duerstock and R. Shi, Hydralazine inhibits compression and acrolein-mediated injuries in ex vivo spinal cord, *J. Neurochem.*, 2008, **104**(3), 708–718.

92 M. A. DeTure and D. W. Dickson, The neuropathological diagnosis of Alzheimer's disease, *Mol. Neurodegener.*, 2019, **14**(1), 32.

93 A. Alzheimer, R. A. Stelzmann, H. N. Schnitzlein and F. R. Murtagh, An English translation of Alzheimer's 1907 paper, "Uber eine eigenartige Erkankung der Hirnrinde", *Clin. Anat.*, 1995, **8**(6), 429–431.

94 A. Metaxas and S. J. Kempf, Neurofibrillary tangles in Alzheimer's disease: elucidation of the molecular mechanism by immunohistochemistry and tau protein phospho-proteomics, *Neural Regener. Res.*, 2016, **11**(10), 1579–1581.

95 H. Braak and E. Braak, Temporal sequence of Alzheimer's disease-related pathology, *Cerebral cortex*, Springer; 1999, pp. 475–512.

96 G. Muntané, E. Dalfó, A. Martinez and I. Ferrer, Phosphorylation of tau and alpha-synuclein in synaptic-enriched fractions of the frontal cortex in Alzheimer's disease, and in Parkinson's disease and related alpha-synucleinopathies, *Neuroscience*, 2008, **152**(4), 913–923.

97 B. E. Hawkins, S. Krishnamurthy, D. L. Castillo-Carranza, U. Sengupta, D. S. Prough and G. R. Jackson, *et al.*, Rapid accumulation of endogenous tau oligomers in a rat model of traumatic brain injury: possible link between traumatic brain injury and sporadic tauopathies, *J. Biol. Chem.*, 2013, **288**(23), 17042–17050.

98 A. Kahriman, J. Bouley, T. W. Smith, D. A. Bosco, A. L. Woerman and N. Henninger, Mouse closed head traumatic brain injury replicates the histological tau pathology pattern of human disease: characterization of a novel model and systematic review of the literature, *Acta Neuropathol. Commun.*, 2021, **9**(1), 118.

99 O. Albayram, A. Kondo, R. Mannix, C. Smith, C. Y. Tsai and C. Li, *et al.*, Cis P-tau is induced in clinical and preclinical brain injury and contributes to post-injury sequelae, *Nat. Commun.*, 2017, **8**(1), 1000.

100 S. R. Shultz, D. K. Wright, P. Zheng, R. Stuchbery, S. J. Liu and M. Sashindranath, *et al.*, Sodium selenate reduces hyperphosphorylated tau and improves outcomes after traumatic brain injury, *Brain*, 2015, **138**(Pt 5), 1297–1313.

101 E. Hill, M. J. Wall, K. G. Moffat and T. K. Karikari, Understanding the Pathophysiological Actions of Tau Oligomers: A Critical Review of Current Electrophysiological Approaches, *Front. Mol. Neurosci.*, 2020, **13**, 155.

102 A. C. McKee and D. H. Daneshvar, The neuropathology of traumatic brain injury, *Handb. Clin. Neurol.*, 2015, **127**, 45–66.

103 Z. Liu, T. Li, P. Li, N. Wei, Z. Zhao and H. Liang, *et al.*, The Ambiguous Relationship of Oxidative Stress, Tau Hyperphosphorylation, and Autophagy Dysfunction in

Alzheimer's Disease, *Oxid. Med. Cell. Longevity*, 2015, **2015**, 352723.

104 T. J. Cohen, J. L. Guo, D. E. Hurtado, L. K. Kwong, I. P. Mills and J. Q. Trojanowski, *et al.*, The acetylation of tau inhibits its function and promotes pathological tau aggregation, *Nat. Commun.*, 2011, **2**, 252.

105 B. Caballero, M. Bourdenx, E. Luengo, A. Diaz, P. D. Sohn and X. Chen, Acetylated tau inhibits chaperone-mediated autophagy and promotes tau pathology propagation in mice, *Nat. Commun.*, 2021, **12**(1), 2238.

106 S. W. Min, S. H. Cho, Y. Zhou, S. Schroeder, V. Haroutunian and W. W. Seeley, *et al.*, Acetylation of tau inhibits its degradation and contributes to tauopathy, *Neuron*, 2010, **67**(6), 953–966.

107 K. Uchida, Current status of acrolein as a lipid peroxidation product, *Trends Cardiovasc. Med.*, 1999, **9**(5), 109–113.

108 T. N. Dang, M. Arseneault, V. Murthy and C. Ramassamy, Potential role of acrolein in neurodegeneration and in Alzheimer's disease, *Curr. Mol. Pharmacol.*, 2010, **3**(2), 66–78.

109 B. B. Timothy, *et al.*, Diffusive secondary injuries in neuronal networks following a blast impact: A morphological and electrophysiological study using a TBI-on-a-Chip model, *Brain Multiphys.*, 2024, **7**, 100104, DOI: **10.1016/j.brain.2024.100104**.

110 D. Pamies, T. Hartung and H. T. Hogberg, Biological and medical applications of a brain-on-a-chip, *Exp. Biol. Med.*, 2014, **239**(9), 1096–1107, DOI: **10.1177/1535370214537738**.

111 S. M. Beltrán, J. Bobo, A. Habib, C. V. Kodavali, L. Edwards, P. Mamindla, R. E. Taylor, P. R. LeDuc and P. O. Zinn, Characterization of neural mechanotransduction response in human traumatic brain injury organoid model, *Sci. Rep.*, 2023, **13**(1), 13536; S. M. Beltrán, J. Bobo, A. Habib, C. V. Kodavali, L. Edwards, P. Mamindla, R. E. Taylor, P. R. LeDuc and P. O. Zinn, Erratum, *Sci. Rep.*, 2024, **14**(1), 2151, DOI: **10.1038/s41598-023-40431-y**, PMID: 37598247; PMCID: PMC10439953.

112 D. Lam, N. O. Fischer and H. A. Enright, Probing function in 3D neuronal cultures: a survey of 3D multielectrode array advances, *Curr. Opin. Pharmacol.*, 2021, **60**, 255–260, DOI: **10.1016/j.coph.2021.08.003**, Epub 2021 Sep 1. PMID: 34481335.